Experimental and Numerical Study of the Dependency of Interface Fracture in Concrete-Rock Specimens on Mode Mixity

Hong Zhong[a], Ean Tat Ooi[b,*], Chongmin Song[c], Tao Ding[a], Gao Lin[a], Hongjun Li[d]

[a] *State Key Laboratory of Coastal and Offshore Engineering, Dalian University of Technology, Dalian 116023, China*
[b] *School of Science, Information Technology and Engineering, Federation University, Ballarat, VIC 3353, Australia*
[c] *School of Civil and Environmental Engineering, The University of New South Wales, NSW 2031, Australia*
[d] *State Key Laboratory of Simulation and Regulation of Water Cycle in River Basin, China Institute of Water Resources and Hydropower Research, Beijing 100048, China*

Abstract

The interface between the concrete and the rock is usually considered the weakest link in concrete structures built in rock foundations. The fracture behaviour at the concrete-rock interface is influenced by many factors e.g. the material properties of the individual constituents, the fracture process zone at the interface and the mode mixity ratio. This paper investigates the dependency of the fracture behaviour of concrete-rock interfaces on the mode mixity ratio using experimental and numerical methods. The experimental program involves four-point-shear of concrete-rock composite beams. It is designed to test a wide range of mode mixity ratio. Using linear elastic fracture mechanics theory, the fracture toughness and the fracture energy are first quantified in terms of the mode mixity ratio. The scaled boundary finite element method, which is known for its accuracy in modeling fracture, is used to compute the fracture toughness and fracture energy. Next, the crack propagation process of the concrete-rock composite beam is modeled using nonlinear fracture mechanics theory. The scaled boundary finite element method is coupled with interface elements to model the fracture process zone, which is a characteristic of fracture in quasi-brittle materials such as concrete and rock. A revised scaled boundary finite element method formulation using generalized coordinates is used to model the cohesive tractions. The cohesive crack at the interface is assumed to propagate when either the Mode 1 or the Mode 2 stress intensity factors change sign. A simple remeshing algorithm is used to propagate the crack at the interface. The numerical simulations are validated by the experimental measurements.

*Corresponding author
Email address: ooi.ean.tat@gmail.com (Ean Tat Ooi)

The simulated crack propagation processes are described in terms of the mode mixity ratio.

Keywords: interface fracture, concrete-rock, mode mixity, cohesive crack model, scaled boundary polygons

---

1. Introduction

Many concrete structures such as concrete dams, gravity wharfs and underground geological repositories for nuclear waste storage are built on rock foundations. The physical properties of concrete and rock are well documented in the literature e.g. [1, 2]. The behavior of the interface between the concrete and the rock, which is generally considered as the weak link of the structure-rock foundation system, however, is not a well understood phenomenon. In the stability analysis of such structures, the assumption of perfect bonding at the concrete-rock interface is usually employed, e.g., [3]. More realistic analyses reported in the literature include the use of friction models to quantify the relative movements between the dam foundation and the dam [4] and spring elements that model the water uplift pressure at the concrete-rock interface [5]. These analyses, however, do not account for the fracture behaviour at the interface. A comprehensive analysis of the stability at the concrete-rock interface requires an in-depth understanding of the behavior of the interfaces between the mortar and the aggregates, which is intrinsic to the concrete and the rock.

Unlike homogeneous materials, the fracture behaviour of a bimaterial interface crack depends on the mode mixity ratio [6]. This has been observed in many experimental studies e.g. [7, 8, 9, 10, 11, 12, 13]. Lee and Buyukozturk [7] reported the fracture toughness curves of the mortar-aggregate interfaces in concrete using sandwiched specimens subjected to four-point-bending and Brazilian disk tests. They observed a remarkable increase of interface fracture toughness with shear loading relative to that of tensile loading. The same authors also observed a similar behaviour in their experimental tests on high strength concrete [8]. In the three-point bending tests on concrete-composite specimens reported by Buyukozturk and Hearing [9], the magnitude of the interface toughness was observed to depend on the mismatch of the elastic moduli and fracture toughness of the aggregate and mortar. Tippur and Rosakis [10], Tippur and Ramaswamy [11] reported the dependence of the interfacial crack initiation toughness and the dynamic fracture behaviour on the crack tip mode mixity parameter for a PMMA-Al bi-material system. Agrawal and Karlsson [12] reported the dependency of the interfacial fracture toughness on the mode mixity ratio for aluminium-vinyl ester specimens subjected to four-point bending. Yang et al. [13] investigated the fracture toughness at the concrete-rock interface using single-notched concrete-rock beams. They found that the Mode 1 fracture toughness of the interface varied with the mode mixity ratio and proposed a failure criterion for the concrete-rock interface that includes the contributions of both Mode 1 and Mode 2 fracture toughness.

The experimental studies aforementioned were performed with the objective of quantifying the fracture toughness over a wide range of mode mixity. This task is, however, very difficult because the complexity of the stress distribution at the bi-material interface. To achieve this objective, numerical methods are usually used to interpret the experimental measurements e.g. [7, 12]. The fracture toughness at the interface is computed using linear elastic fracture mechanics theory [7, 8, 9, 10, 11, 12, 13] under the assumption that it is valid for the loading and specimen sizes tested. The accurate modeling of the fracture behaviour at bi-material interfaces, however, is a very challenging problem in computational mechanics.

Unlike homogeneous materials, the variation of the normal and shear stresses on the interface are coupled when the theory of linear elastic fracture mechanics is used. The orders of singularity at the bi-material interface crack appear as a pair of complex conjugates $0.5 \pm i\varepsilon$. The polynomial shape functions used in the standard finite element method cannot effectively model the stress field in the vicinity of the crack tip Shih and Asaro [14], Matos et al. [15] unless a very fine mesh is employed. To avoid local mesh refinement at the crack tip, special singular finite elements e.g. Lin and Mar [16] or local enrichment functions e.g. Sukumar et al. [17] that incorporate the asymptotic expansion at a bi-material crack formulated by Williams [18] have to be used.

The assumption of linear elastic fracture mechanics in the numerical simulations, however, is inadequate to capture the nonlinear strain softening behaviour observed in the fracture of quasi-brittle material such as concrete and rock. This nonlinearity arises from the development of a fracture process zone along the crack surfaces where normal and shear stresses act through mechanisms such as aggregate interlocking and surface friction. Therefore, a more realistic analysis of the fracture at the concrete-rock interface requires the use of nonlinear fracture mechanics. Similar to linear elastic fracture, the simulation of nonlinear cohesive fracture with the standard finite element method requires the use of very fine meshes in the vicinity of the cracks unless the formulation is augmented by the asymptotic expansions for cohesive cracks e.g. Karihaloo and Xiao [19] and Alberto and Valente [20].

This paper investigates fracture toughness at a concrete-rock interface, with special emphasis on its relation with the mode mixity using both experimental and numerical approaches. Composite beam specimens with a concrete-rock interface are tested under four-point-shear loading conditions. The experimental program is designed to enable a wide range of mode mixity ratio to be tested. Numerical simulations are used to interpret the experimental results. The numerical simulations consist of two parts. The first part attempts to quantify the fracture toughness and the fracture energy of the concrete-rock interface under the assumption of linear elastic fracture mechanics. This validity of this assumption is supported by the almost linear structural response observed by Lee and Buyukozturk [7] in aggregate-mortar interfaces before the ultimate load bearing capacity has been reached. In the second part, the nonlinear fracture behaviour of the concrete-rock interface is modeled. The measured experimental data are used to calibrate the parameters of the traction-separation curve of

the fracture process zone, which is characteristic of quasi-brittle materials such as rock and concrete. The numerical simulations are then validated using the experimental measurements.

To enable accurate interpretation and quantification of the experimental results, the numerical simulations are performed using the scaled boundary finite element method [21]. The scaled boundary finite element method is a semi-analytical technique with unique features that makes it particularly suitable to simulate the fracture behaviour at bi-material interfaces:

1. The stress field around the crack tip, which includes the singular stresses and higher order terms, is analytically represented in the scaled boundary finite element solutions [22]. Therefore, for numerical simulations within the framework of linear elastic fracture mechanics, the stress intensity factors can be accurately computed from their definitions. A fine mesh at the crack tip as in the finite element method e.g. [23] is not required. It does not require local enrichment functions at the crack tip such as in the extended finite element method e.g. [24]. This leads to an accurate procedure to compute the interface toughness at stress concentrations in material junctions.
2. The scaled boundary finite element method can also be conveniently coupled with interface elements to model cohesive fracture in quasi-brittle materials [25]. When cohesive cracks are modeled, the asymptotic stress field in the vicinity of the crack tip [19, 26] is also analytically represented by the scaled boundary finite element solution. This enables accurate modeling of cohesive fracture problems without the need for local mesh refinement. In this paper, a revised scaled boundary formulation using generalized coordinates to treat the cohesive tractions based on a similar one developed by Song [27]. This approach is more robust and does not require the arbitrary shifting of the exponents in the cohesive tractions reported by Yang and Deeks [28].
3. The scaled boundary finite element method can be formulated on polygons of arbitrary number of sides, which makes mesh generation more flexible. Additionally, it leads to simple remeshing algorithms when modeling crack propagation [29].

This paper is organized as follows. In Section 2, the experimental program is described in detail. Section 3 discusses the results that are measured from the experiments. Section 4 describes the numerical method that is used to interpret the experimental measurements. In Section 5, the interface fracture toughness of the concrete-rock specimens are quantified in terms of the mode mixity ratio. In Section 6 the fracture behaviour at the concrete-rock interface is investigated using nonlinear fracture mechanics. The parameters of the cohesive crack model at the bi-material interface are calibrated from the experimentally measured load-deformation responses with the help of the numerical simulations. The crack propagation process of the concrete-rock specimens are modeled to validate the numerical approach. The major conclusions of this study are summarized in Section 7.

2. Experimental program

The experimental program was designed to investigate the fracture behavior at the concrete-rock interface under a wide range of mode mixity ratio. A series of concrete-rock composite beams with an interface crack as shown in Fig. 1 were tested under four-point shear on a universal material test rig. The experiments were performed in the State Key Laboratory of Coastal and Offshore Engineering in Dalian University of Technology.

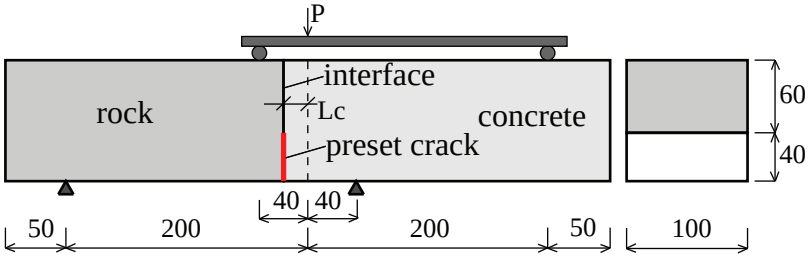

Figure 1: Four-point shear loading of concrete-rock specimens (unit: mm).

2.1. Design of specimens

The dimensions of the concrete-rock composite beams are 500mm×100mm×100mm. The loading span is 400mm. The length of the preset crack at the material interface is 40mm. A wide range of mode mixity ratio can be investigated by varying the length of the rock section L_{rock} of the beam. In this experimental program, composite beams with L_{rock} ranging from 210mm–250mm were tested. For each L_{rock} considered, four sets of specimens were fabricated.

The specimens were fabricated by first incising granite mass rocks to the appropriate lengths L_{rock}. The cross sectional surfaces of the rock were roughened by introducing grooves with an average width of 3mm using a saw as shown in Fig. 2. This conforms to standard practice in engineering in which the concrete-rock interface is treated to increase its surface roughness. It also accounts for the influence of the surface roughness at the concrete-rock interface which affects its fracture behavior. The surface roughness introduced by this process is uniform throughout the cross-sections of all specimens.

The incised rocks are then placed inside molds where concrete mixtures were cast on to them to the full length of the composite beams. The specimens were taken out of the molds three days after casting and allowed to cure under room temperature and humidity conditions for 28 days before testing.

2.2. Material properties

In order for the results of the experimental program to be of practical use in the safety evaluation of concrete structures built on rock foundations, the materials (rock and concrete) commonly used for the construction of these structures

Figure 2: Roughening of rock portion at the interface.

are selected. The Young's modulus E and the Poisson's ratio ν were determined from a 1000kN hydraulic universal testing machine.

For the rock, sections of the prisms with dimensions $50\text{mm} \times 50\text{mm} \times 100\text{mm}$ were incised from uniform granite mass rock. The measured material properties of the rock are listed in Table 1.

The mixture proportions of the concrete are cement 1: water 0.5 : fine aggregates 1.13: coarse aggregates 2.28. The Young's modulus and Poisson's ratio of concrete were measured from $150\text{mm} \times 150\text{mm} \times 300\text{mm}$ concrete prisms after 28 days of curing under room temperature. The measured material properties are listed in Table 1.

Table 1: Measured material properties of concrete and rock.

	E (GPa)	ν
Rock	18.1	0.323
Concrete	27.85	0.178

2.3. Four-point shear tests

A closed loop servo-controlled testing machine with a capacity of 100kN was used for the four-point-shear tests. The ratio of loads on the two loading points is 1:5. A calibrated 50kN load cell is used to measure the load. The loading-point displacement is measured using a linear variable differential transformer. The crack mouth opening displacement (CMOD) and the crack mouth sliding displacement (CMSD) were measured using a clip gage. The experimental setup for the four-point shear test is shown in Fig. 3. The beams were tested under displacement control. The displacement at the loading point was used as the control parameter and was increased monotonically throughout the test.

Figure 3: Experiment setup for four point shear test.

Compared with the experimental program reported by Lee and Buyukozturk [7, 8], which required both four-point bending and Brazillian disk tests to enable mode mixity angles between $0^\circ - 90^\circ$ to be covered, a four-point-shear test simplifies the specimen preparation and testing process. The same set of molds and loading apparatus can be used for all specimens. A wide range of mode mixity can be generated by a simple change in L_{rock}. This reduces the time required for specimen preparation.

Another unique feature of the four-point shear test is that the mode mixity is only weakly dependent on the length of the preset crack [30]. Therefore, the mode mixity angle of the beam remains almost constant throughout the crack propagation process. The fracture process can therefore be quantified in terms of the initial mode mixity angles.

3. Experimental results

The outputs from the experimental program include the loading responses of the specimens i.e. $P-\text{CMOD}$ and $P-\text{CMSD}$ curves and the maximum load $P^{\max}$, and the failure modes of each specimen. In this section, the physically observed failure modes and the general behaviour of the loading responses of the specimens are described. Quantification of the experimental results in terms of the mode mixity of the specimens are presented together with the numerical simulations in Sections 5-6.2.

3.1. Failure modes

During the experiments, three types of failure modes were observed: interface cracking along the concrete-rock interface (I), interface cracking followed by crack kinking into the rock (IR) and interface cracking followed by brittle failure near the concrete support (IC).

1. *Interface failure along the concrete-rock interface (I).* Fig. 4a shows an example of this failure mode. This failure mode is generally observed in specimens with low values of L_{rock} i.e. 210mm $\leq L_{\text{rock}} \leq$ 225mm. In these specimens, the eccentricity of the loading point and the interface is relatively small. The bending moment at the concrete-rock interface is positive and the tensile stress is much larger than the shear stress. Therefore, the crack propagates in almost a straight line along the concrete-rock interface up to failure. As the concrete-rock interface is the weakest link in the composite beam, this failure mode is to be expected.
2. *Interface cracking followed by crack kinking into the rock (IR).* Fig. 4b shows an example of this failure mode, which observed in specimens with large values of L_{rock} i.e. $L_{\text{rock}} \geq$ 245mm. In these specimens, the bending moment at the concrete-rock interface decreases. Therefore, the magnitude of the tensile stress is much smaller than the shear stress. The crack propagation process is initially a straight line along the weak interface. When the crack reaches the middle of the beam a secondary crack developed and kinked into the rock, which could possibly be a result of a large shear stress at the crack tip. The primary crack continued to propagate along the interface until failure.
3. *Interface cracking followed by brittle failure near the concrete support (IC).* This failure mode is observed in specimens with 230mm $\leq L_{\text{rock}} \leq$ 245mm. Fig. 4c shows an example of this failure mode. In these specimens, the crack propagated along the interface. As the interface crack approached the top edge of the specimen, a secondary crack was observed to initiate near the concrete support. This was then followed by sudden brittle failure at the concrete support. This failure mode, which is commonly observed in conventional four-point shear tests of homogeneous materials [31], was observed in the experiments because the mechanical properties of concrete and rock are relatively similar.

In general, specimens with lower magnitudes of L_{rock} fail due to crack propagation along the concrete-rock interface. When L_{rock} is increased, the failure modes IC and IR were observed more frequently. Table 2 shows the failure modes and measured peak loads of all the specimens tested. The specimens are named according to the their respective L_{rock}. For every L_{rock}, each of the four specimens are numbered sequentially. For example, the second specimen for a beam with $L_{\text{rock}} =$ 215mm is named 215-2. The crack faces, as shown in Figs. 5a and 5b, are rather smooth, which indicates that the concrete-rock interface is a weak one.

3.2. Load and deformation

Fig. 6a shows the $P -$ CMOD and $P -$ CMSD curves for a specimen with $L_{\text{rock}} =$ 215mm. After the disturbance at the initial stage of loading, the magnitudes of both the CMOD and CMSD increased with the load. The peak load

Table 2: Measured peak load and failure mode of specimens.

L_{rock}(mm)	Specimen	Failure mode	$P^{\max}$(kN)
210	210-2	I	8.97
	210-3	I	9.89
	210-4	I	14.1
215	215-1	I	12.71
	215-2	I	16.06
	215-3	I	14.26
	215-4	I	16.16
220	220-1	I	17.71
	220-2	I	8.26
	220-3	I	12.47
	220-4	I	12.31
225	225-2	I	12.31
	225-3	I	6.43
	225-4	I	18.15
230	230-3	I	15.36
	230-4	IC	20.01
235	235-3	IC	26.41
	235-4	I	21.17
240	240-2	IC	23.67
	240-4	I	22.40
245	245-1	IC	31.09
	245-2	IC	23.51
	245-3	IR	25.81
250	250-1	IR	27.72
	250-4	I	20.41

(a) interface failure (I)

(b) interface cracking and kinking into rock (IR)

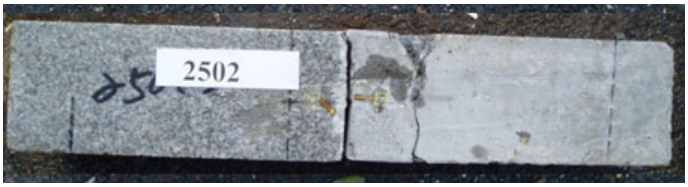

(c) interface cracking and brittle failure near concrete support (IC)

Figure 4: Observed failure modes in experimental program.

$P^{\max}$ was 16.06kN for this specimen. After $P^{\max}$ has been reached, the crack started to propagate unstably until the specimen failed. The experiment was not able to capture the load response after the peak load has been reached. This, however, can be modeled using nonlinear fracture mechanics as will be shown in the numerical simulations in Section 6.2. The $P-$CMOD and $P-$CMSD curves of the other specimens tested in the experimental program show similar trends. They differ only in the magnitudes of the measured $P^{\max}$, CMOD, CMSD and the slope during pre-peak response.

4. Numerical simulations

In this paper, numerical simulations are used to: (i) evaluate the fracture toughness and determine its dependency on the mode mixity ratio; (ii) determine an empirical relation for the fracture energy of the concrete-rock interface; and (iii) calibrate the cohesive crack model of the concrete of the concrete-rock interface. The numerical simulations performed in this study consists of two parts. In the first part, linear elastic fracture mechanics theory is used to compute the fracture toughness and the fracture energy of the interface and quantify their variation in terms of the mode mixity ratio. In the second part, nonlinear

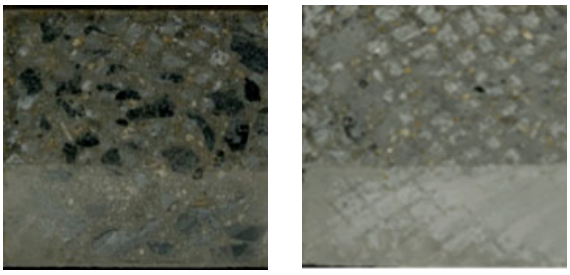

(a) rock (b) concrete

Figure 5: Crack surfaces at the interface.

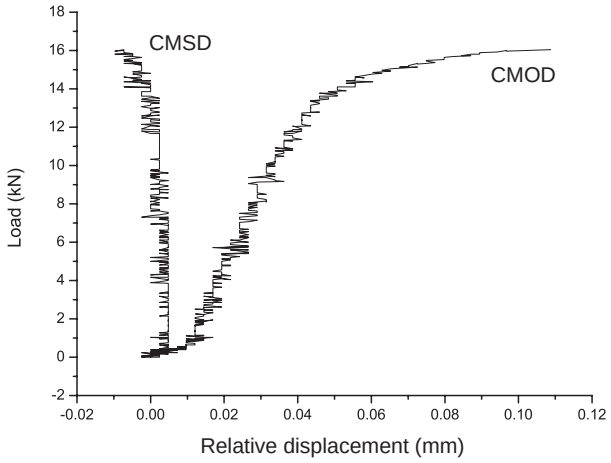

Figure 6: Typical load-displacement curves.

fracture mechanics theory is used to model the strain softening behaviour at the interface, which is a characteristic of fracture in quasi-brittle materials such as concrete and rock.

To facilitate the modeling of such fracture problems, the scaled boundary polygons developed by Ooi et al. [29, 25] is employed. This approach is particularly suited to model the both linear and nonlinear fracture at the bi-material interfaces because:

1. The asymptotic expansion, which include the stress singularity and higher order terms, in the vicinity of the crack is analytically represented in its solutions. Therefore, within the framework of linear elastic fracture mechanics, and nonlinear fracture mechanics, respectively, the singular stress field in the vicinity of the crack tip and the fracture processes that are characterized by nonlinear cohesive zones can be modeled accurately without the need for local mesh refinement.
2. Within the framework of nonlinear fracture mechanics, the process zone can be easily incorporated into the scaled boundary polygons using cohesive crack models and zero-thickness interface elements.
3. The computational domain can be flexibly meshed by polygons with arbitrary number of sides. This leads to simple remeshing algorithms to model crack propagation.

The saled boundary polygon formulation is first presented for the case with tractions acting on the side-faces of the crack. The revised formulation using generalized coordinates developed by Song [27] is used. The special case of linear elastic fracture mechanics where the crack faces are traction-free is presented in Section 4.2. Its extension to model nonlinear cohesive fracture is presented in Section 4.3.

4.1. Scaled boundary polygon formulation

The basic theory and formulations of the scaled boundary polygons relevant to fracture are presented for the sake of completeness. Detailed formulations of the method can be referred to in Song [27].

4.1.1. Geometric representation

The scaled boundary finite element method [21] can be formulated on polygons with arbitrary number of sides. The geometry of a polygon has to only satisfy a so-called scaling requirement i.e. the entire boundary has to be visible from a point inside the domain. This requirement can always be satisfied by subdividing a subdomain to smaller ones. Fig. 7a and Fig. 7b show the scaled boundary coordinates of an arbitrary n-sided polygon and a polygon modeling a bi-material crack, respectively.

In a normal polygon, the scaling centre O is chosen at the geometric center. A radial coordinate ξ is defined in the polygon. ξ takes a value of 0 at the scaling center and 1 at the polygon's boundary. The polygon boundary is discretized with standard one-dimensional finite elements. In each element, a

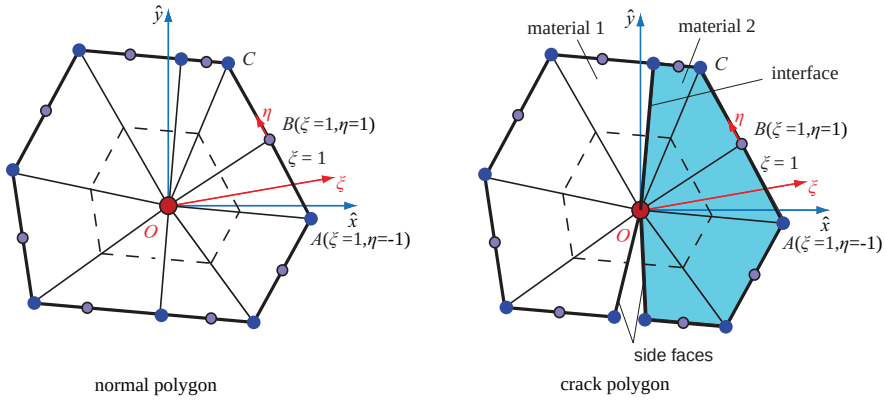

Figure 7: Polygon representation of a crack.

local coordinate η that varies from -1 to $+1$ is defined as in the finite element method.

In the cracked polygon, the scaling center O is chosen at the crack tip. The crack edges are formed by scaling the nodes A and B on the boundary and are not discretized. Similarly, the material interface is also formed by scaling.

The global Cartesian coordinate for a point with scaled boundary coordinate system (ξ, η) is expressed as

$$\left\{ \begin{array}{c} \hat{x}(\xi,\eta) \\ \hat{y}(\xi,\eta) \end{array} \right\} = \xi \mathbf{N}(\eta) \left\{ \begin{array}{c} \mathbf{x}_\mathrm{b} \\ \mathbf{y}_\mathrm{b} \end{array} \right\} \tag{1}$$

where

$$\mathbf{N}(\eta) = \left[\begin{array}{cccccccc} N_1(\eta) & 0 & N_2(\eta) & 0 & \dots & 0 & N_M(\eta) & 0 \\ 0 & N_1(\eta) & 0 & N_2(\eta) & & \dots & 0 & N_M(\eta) \end{array} \right] \tag{2}$$

is the shape function matrix with M number of nodes, $\mathbf{x}_\mathrm{b}$ and $\mathbf{y}_\mathrm{b}$ are the vector of nodal coordinates of the element.

4.1.2. Displacement and stress interpolation

Along the radial direction, nodal displacement functions $\mathbf{u}(\xi)$ are introduced. The displacement at any point in a polygon is expressed as

$$\mathbf{u}(\xi,\eta) = \mathbf{N}(\eta)\mathbf{u}(\xi) \tag{3}$$

The stress vector is

$$\boldsymbol{\sigma}(\xi,\eta) = \mathbf{D}\mathbf{B}_1(\eta)\mathbf{u}(\xi)_{,\xi} + \xi^{-1}\mathbf{D}\mathbf{B}_2(\eta)\mathbf{u}(\xi) \tag{4}$$

where $\mathbf{D}$ is the elasticity constitutive matrix of the material. $\mathbf{B}_1$ and $\mathbf{B}_2$ are the strain displacement matrices (see Wolf [21]).

4.1.3. Scaled boundary formulation

Following the approach of Wolf [21] and applying the Galerkin's weighted residual technique, the equilibrium condition in a polygon is given by the scaled boundary finite element equation in displacement

$$\mathbf{E}_0\xi^2\mathbf{u}(\xi)_{,\xi\xi} + (\mathbf{E}_0 - \mathbf{E}_1 + \mathbf{E}_1^{\mathrm{T}})\xi\mathbf{u}(\xi)_{,\xi} - \mathbf{E}_2\mathbf{u}(\xi) + \mathbf{F}(\xi) = 0 \tag{5}$$

In this equation, $\mathbf{E}_i$, $i = 0, 1, 2$ are coefficient matrices that depend only on the geometry and material properties of an element sector in the polygon and $\mathbf{F}(\xi)$ is the load vector that contains contribution from the cohesive forces acting on the side-faces of a cracked polygon. $\mathbf{F}(\xi)$ can be expressed as a power function in the radial coordinate ξ [32] as

$$\mathbf{F}(\xi) = \xi^b\mathbf{F}_{\mathrm{t}} \tag{6}$$

with $b = d + 1$.

The internal nodal forces along the radial lines are equal to

$$\mathbf{q}(\xi) = \mathbf{E}_0\xi\mathbf{u}(\xi)_{,\xi} + \mathbf{E}_1^{\mathrm{T}}\mathbf{u}(\xi) \tag{7}$$

Eq. (5) is a system of linear nonhomogeneous second-order ordinary differential equations for the displacement functions $\mathbf{u}(\xi)$. It can be transformed into a first order ordinary differential equation with twice the number of unknowns [27] by introducing the variable

$$\mathbf{X}(\xi) = \left\{ \begin{array}{c} \mathbf{u}(\xi) \\ \mathbf{q}(\xi) \end{array} \right\} \tag{8}$$

so that Eq. (5) becomes

$$\xi\mathbf{X}(\xi)_{,\xi} = -\mathbf{Z}\mathbf{X}(\xi) - \left\{ \begin{array}{c} 0 \\ \mathbf{F}(\xi) \end{array} \right\} \tag{9}$$

with the coefficient matrix

$$\mathbf{Z} = \left[\begin{array}{cc} \mathbf{E}_0^{-1}\mathbf{E}_1^{\mathrm{T}} & \mathbf{E}_0^{-1} \\ -\mathbf{E}_2 + \mathbf{E}_1\mathbf{E}_0^{-1}\mathbf{E}_1^{\mathrm{T}} & -\mathbf{E}_1\mathbf{E}_0^{-1} \end{array} \right] \tag{10}$$

The Hamiltonian matrix $\mathbf{Z}$ satisfies the identity [27]

$$(\mathbf{J}_{2\mathrm{n}}\mathbf{Z})^{\mathrm{T}} = \mathbf{J}_{2\mathrm{n}}\mathbf{Z} \tag{11}$$

where $\mathbf{J}_{2\mathrm{n}}$ is defined as

$$\mathbf{J}_{2\mathrm{n}} = \left[\begin{array}{cc} 0 & -\mathbf{I} \\ \mathbf{I} & 0 \end{array} \right] \tag{12}$$

and $\mathbf{I}$ is an identity matrix.

4.1.4. Solution for side-face tractions varying as power functions in ξ

A block diagonal Schur decomposition of $\mathbf{Z}$ in Eq. (10) results in the following Schur matrix $\mathbf{S}$ and transformation matrix $\mathbf{\Psi}$ for a polygon [27]

$$\mathbf{Z}\mathbf{\Psi} = \mathbf{\Psi}\mathbf{S} \tag{13}$$

with

$$\mathbf{S} = \text{diag}\left(\begin{array}{cccccccc} \mathbf{S}_1, & \ldots & \mathbf{S}_{N-1}, & \left[\begin{array}{cc} \mathbf{S}_N & \mathbf{I} \\ 0 & \mathbf{S}_{N+1} \end{array} \right], & \mathbf{S}_{N+2}, & \ldots & \mathbf{S}_{2N} \end{array} \right) \tag{14}$$

where $\mathbf{S}_N = \mathbf{S}_{N+1} = 0$. The diagonal entries of $\mathbf{S}$ are equal to the real parts of the eigenvalues of $\mathbf{Z}$. The $2N$ diagonal blocks of $\mathbf{S}$ form N pairs of conjugate $\mathbf{S}_i$ and $\mathbf{S}_{\bar{\imath}}$ where the index of the block conjugate to the ith block is

$$\bar{\imath} = 2N + 1 - i \tag{15}$$

The transformation matrix $\mathbf{\Psi}$ is

$$\mathbf{\Psi} = \left[\begin{array}{ccccccc} \mathbf{\Psi}_1, & \ldots, & \mathbf{\Psi}_{N-1}, & \mathbf{\Psi}_N, & \mathbf{\Psi}_{N+1}, & \ldots & \mathbf{\Psi}_{2N} \end{array} \right] \tag{16}$$

and is $\mathbf{J}_{2n}$-orthogonal [27]

$$\mathbf{\Psi}_i^{\mathrm{T}} \mathbf{J}_{2n} \mathbf{\Psi}_j = -\left(\mathbf{\Psi}_j^{\mathrm{T}} \mathbf{J}_{2n} \mathbf{\Psi}_i\right)^{\mathrm{T}} = \left\{ \begin{array}{cc} \mathbf{H}_i & \text{when } j = \bar{\imath} \\ 0 & \text{when } j \neq \bar{\imath} \end{array} \right. \tag{17}$$

Pre-multiplying Eq. (13) with $-\mathbf{\Psi}_{\bar{\imath}}^{\mathrm{T}} \mathbf{J}_{2n}$ and using Eq. (17) results in

$$-\mathbf{\Psi}_{\bar{\imath}}^{\mathrm{T}} \mathbf{J}_{2n} \mathbf{Z} \mathbf{\Psi}_j = \left\{ \begin{array}{cc} \mathbf{H}_i^{\mathrm{T}} & \text{when } j = i \\ 0 & \text{when } j \neq i \end{array} \right. \tag{18}$$

The unknown functions $\mathbf{X}(\xi)$ are decomposed with the transformation matrix $\mathbf{\Psi}$ as base functions [27]

$$\mathbf{X}(\xi) = \mathbf{\Psi}\mathbf{W}(\xi) \tag{19}$$

where $\mathbf{W}(\xi)$ are the generalized coordinate functions. The base functions $\mathbf{\Psi}$ can be partitioned into two row blocks with equal size $\mathbf{\Psi}^{(\mathrm{u})}$ and $\mathbf{\Psi}^{(\mathrm{q})}$ and further into four square matrices of size $n \times n$ as

$$\mathbf{\Psi} = \left[\begin{array}{c} \mathbf{\Psi}^{(\mathrm{u})} \\ \mathbf{\Psi}^{(\mathrm{q})} \end{array} \right] = \left[\begin{array}{cc} \mathbf{\Psi}_{\mathrm{n}}^{(\mathrm{u})} & \mathbf{\Psi}_{\mathrm{p}}^{(\mathrm{u})} \\ \mathbf{\Psi}_{\mathrm{n}}^{(\mathrm{q})} & \mathbf{\Psi}_{\mathrm{p}}^{(\mathrm{q})} \end{array} \right] \tag{20}$$

Using Eqs. (19) and (20), the radial displacement functions $\mathbf{u}(\xi)$ and the nodal internal forces $\mathbf{q}(\xi)$ can be expressed as

$$\mathbf{u}(\xi) = \mathbf{\Psi}^{(\mathrm{u})} \mathbf{W}(\xi) \tag{21}$$

$$\mathbf{q}(\xi) = \mathbf{\Psi}^{(\mathrm{q})} \mathbf{W}(\xi) \tag{22}$$

For the diagonal blocks with real parts of eigenvalues satisfying $\lambda(\mathbf{S}_i) \neq 0$, substituting Eq. (19) into Eq. (9) pre-multiplied by $-\boldsymbol{\Psi}_i^{\mathrm{T}}\mathbf{J}_{2\mathrm{n}}$ and using Eqs. (17) and (18) leads to [27]

$$\xi\mathbf{W}_i(\xi)_{,\xi} = -\mathbf{S}_i\mathbf{W}_i(\xi) - \mathbf{F}_i^{(\mathrm{w})}(\xi) \tag{23}$$

When the cohesive tractions are expressed in the form of power functions as in Eq. (6), the term $\mathbf{F}_i^{(\mathrm{w})}(\xi)$ can be expressed as

$$\mathbf{F}_i^{(\mathrm{w})}(\xi) = -\mathbf{H}_i^{-\mathrm{T}}(\boldsymbol{\Psi}_{\bar{i}}^{(\mathrm{u})})^{\mathrm{T}}\mathbf{F}_{\mathrm{t}}\xi^b = \overline{\mathbf{F}}_i^{(\mathrm{w})}\xi^b \tag{24}$$

The solution of Eq. (23) is

$$\mathbf{W}_i(\xi) = \xi^{-\mathbf{S}_i}\left(\mathbf{c}_i - \int_1^{\xi} \tau^{-\mathbf{S}_i-\mathbf{I}}\mathbf{F}_i^{(\mathrm{w})}(\xi)d\tau\right) \tag{25}$$

For bounded domains i.e. polygons satisfying $0 \leq \xi \leq 1$, the condition for the finiteness of the displacement functions $\mathbf{u}(\xi)$ and internal nodal forces $\mathbf{q}(\xi)$ requires that $\mathbf{W}(\xi = 0)$ remain finite. For the diagonal blocks with positive real parts of eigenvalues i.e. the last $N-1$ diagonal blocks in Eq. (14), this condition is satisfied by setting the terms in brackets in Eq. (25) to zero. This determines the integration constants $\mathbf{c}_i$ as

$$\mathbf{c}_i = \int_1^0 \tau^{-\mathbf{S}_i-\mathbf{I}}\mathbf{F}_i^{(\mathrm{w})}(\tau)d\tau \quad \text{when } \mathrm{Re}(\lambda(\mathbf{S}_i)) > 0 \tag{26}$$

Substituting Eq. (24) into Eq. (26) and integrating analytically results in the particular solution [27]

$$\mathbf{W}_i(\xi) = \mathbf{W}_i^{(\mathrm{p})}(\xi) = -(\mathbf{S}_i + b\mathbf{I})^{-1}\overline{\mathbf{F}}_i^{(\mathrm{w})}\xi^b \quad \text{when } \mathrm{Re}(\lambda(\mathbf{S}_i)) > 0 \tag{27}$$

For the diagonal blocks with negative real parts of eigenvalues i.e. the first $N-1$ diagonal blocks in $\mathbf{S}$, Eq. (25) satisfies the condition of finiteness at $\xi = 0$ for any $\mathbf{c}_i$. It is split into two parts consisting of a homogeneous and a particular solution as

$$\mathbf{W}_i(\xi) = \xi^{-\mathbf{S}_i}\mathbf{c}_i + \mathbf{W}_i^{(\mathrm{p})}(\xi) \tag{28}$$

The particular solution is obtained by substituting Eq. (24) into Eq. (25) and integrating analytically in ξ, resulting in

$$\mathbf{W}_i^{(\mathrm{p})}(\xi) = -(\mathbf{S}_i + b\mathbf{I})^{-1}\overline{\mathbf{F}}_i^{(\mathrm{w})}\xi^b \quad \text{when } \mathrm{Re}(\lambda(\mathbf{S}_i)) < 0$$

For the diagonal blocks with zero eigenvalues in Eq. (14), the solution for $\mathbf{W}(\xi)$ is obtained following a similar procedure as for the diagonal blocks satisfying $\lambda(\mathbf{S}_i) \neq 0$, which leads to [27]

$$\mathbf{W}_N(\xi) = \mathbf{c}_N + \mathbf{W}_N^{(\mathrm{p})}(\xi) \quad \text{when } \mathbf{S}_N = \mathbf{S}_{N+1} = 0 \tag{29}$$

$$\mathbf{W}_{N+1}(\xi) = \mathbf{W}_{N+1}^{(\mathrm{p})}(\xi) \qquad \text{when } \mathbf{S}_N = \mathbf{S}_{N+1} = 0 \tag{30}$$

The particular solutions are obtained by substituting Eq. (24) into Eq. (25) and then integrating analytically with respect to ξ, resulting in

$$\mathbf{W}_N^{(\mathrm{p})}(\xi) = -\, b^{-1} \left(\overline{\mathbf{F}}_N^{(\mathrm{w})} - b^{-1} \overline{\mathbf{F}}_{N+1}^{(\mathrm{w})} \right) \xi^b \quad \text{when } \mathbf{S}_N = \mathbf{S}_{N+1} = 0 \tag{31}$$

$$\mathbf{W}_{N+1}^{(\mathrm{p})}(\xi) = -\, b^{-1} \overline{\mathbf{F}}_{N+1}^{(\mathrm{w})} \xi^b \qquad \text{when } \mathbf{S}_N = \mathbf{S}_{N+1} = 0 \tag{32}$$

Eqs. (27)-(32) can be used to evaluate the particular solutions when b is sufficiently disjoint from $\lambda(-\mathbf{S}_i)$. When b is close to or equal to $\lambda(-\mathbf{S}_i)$, a stable approach to evaluate the particular solution is obtained by augmenting Eq. (23) as [27]

$$\xi \left\{ \begin{array}{c} \mathbf{W}_i(\xi) \\ \xi^b \end{array} \right\}_{,\xi} = \left[\begin{array}{cc} -\mathbf{S}_i & \overline{\mathbf{F}}_i^{(\mathrm{w})} \\ 0 & b \end{array} \right] \left\{ \begin{array}{c} \mathbf{W}_i(\xi) \\ \xi^b \end{array} \right\} \tag{33}$$

The particular solution $\mathbf{W}_i^{(\mathrm{p})}(\xi)$ is obtained by evaluating the matrix function

$$\xi \left[\begin{array}{cc} -\mathbf{S}_i & \overline{\mathbf{F}}_i^{(\mathrm{w})} \\ 0 & b \end{array} \right] = \left[\begin{array}{cc} \xi^{-\mathbf{S}_i} & \mathbf{W}_i^{(\mathrm{p})}(\xi) \\ 0 & \xi^b \end{array} \right] \tag{34}$$

4.1.5. Stiffness matrix and equivalent nodal force vector

Once the particular solutions have been determined, the displacement functions $\mathbf{u}(\xi)$ and internal nodal forces $\mathbf{q}(\xi)$ can be written in terms of the generalized coordinates as

$$\mathbf{u}(\xi) = \mathbf{\Psi}_{\mathrm{n}}^{(\mathrm{u})} \xi^{-\mathbf{S}} \mathbf{c} + \mathbf{\Psi}^{(\mathrm{u})} \mathbf{W}^{(\mathrm{p})}(\xi) \tag{35}$$

$$\mathbf{q}(\xi) = \mathbf{\Psi}_{\mathrm{n}}^{(\mathrm{q})} \xi^{-\mathbf{S}} \mathbf{c} + \mathbf{\Psi}^{(\mathrm{q})} \mathbf{W}^{(\mathrm{p})}(\xi) \tag{36}$$

The integration constants $\mathbf{c}$ depend on the boundary conditions at $\xi = 1$. The solutions at $\xi = 1$ can be written as

$$\mathbf{u}(\xi = 1) = \mathbf{\Psi}_{\mathrm{n}}^{(\mathrm{u})} \xi^{-\mathbf{S}} \left(\mathbf{c} + \mathbf{W}_{\mathrm{n}}^{(\mathrm{p})}(\xi = 1) \right) + \mathbf{\Psi}_{\mathrm{p}}^{(\mathrm{u})} \mathbf{W}_{\mathrm{p}}^{(\mathrm{p})}(\xi = 1) \tag{37}$$

$$\mathbf{q}(\xi = 1) = \mathbf{\Psi}_{\mathrm{n}}^{(\mathrm{q})} \xi^{-\mathbf{S}} \left(\mathbf{c} + \mathbf{W}_{\mathrm{n}}^{(\mathrm{p})}(\xi = 1) \right) + \mathbf{\Psi}_{\mathrm{p}}^{(\mathrm{q})} \mathbf{W}_{\mathrm{p}}^{(\mathrm{p})}(\xi = 1) \tag{38}$$

using the partition of $\mathbf{\Psi}$ in Eq. (20). Substituting Eq. (37) into Eq. (38) results in

$$\mathbf{q}(\xi = 1) = \mathbf{K}\mathbf{u}(\xi = 1) - \mathbf{R}_{\mathrm{F}} \tag{39}$$

where $\mathbf{K}$ is the stiffness matrix

$$\mathbf{K} = \mathbf{\Psi}_{\mathrm{n}}^{(\mathrm{q})} \left(\mathbf{\Psi}_{\mathrm{n}}^{(\mathrm{u})} \right)^{-1} \tag{40}$$

and $\mathbf{R}_{\mathrm{F}}$ is the nodal load vector due to the side-face traction

$$\mathbf{R}_{\mathrm{F}} = -\left(\mathbf{\Psi}_{\mathrm{n}}^{(\mathrm{q})} - \mathbf{K} \mathbf{\Psi}_{\mathrm{p}}^{(\mathrm{u})} \right) \mathbf{W}_{\mathrm{p}}^{(\mathrm{p})}(\xi = 1) \tag{41}$$

The integration constants c_i can be evaluated using Eq. (35) once $\mathbf{u}(\xi = 1)$ has been determined.

The complete solution for the displacements is obtained by substituting Eq. (35) into Eq. (3). This leads to

$$\mathbf{u}(\xi,\eta) = \mathbf{N}(\eta)\left(\boldsymbol{\Psi}_{\mathrm{n}}^{(\mathrm{u})}\xi^{-\mathbf{S}}\mathbf{c} + \boldsymbol{\Psi}^{(\mathrm{u})}\mathbf{W}^{(\mathrm{p})}(\xi)\right) \tag{42}$$

The stresses $\boldsymbol{\sigma}(\xi,\eta)$ are obtained by substituting Eq. (35) into Eq. (4) resulting in

$$\begin{aligned}\boldsymbol{\sigma}(\xi,\eta) =& \sum_{i=1}^{N} \boldsymbol{\Psi}_{\sigma_i}(\eta)\xi^{-\mathbf{S}_i-\mathbf{I}}\mathbf{c}_i \\ &+ \sum_{i=1}^{2N} \xi^{-1}\left(\boldsymbol{\Psi}_{\sigma_i}(\eta)\mathbf{W}_i^{(\mathrm{p})}(\xi) - \mathbf{D}\mathbf{B}_1(\eta)\boldsymbol{\Psi}_i^{(\mathrm{u})}\overline{\mathbf{F}}_i^{(\mathrm{w})}(\xi)\right)\end{aligned} \tag{43}$$

where $\boldsymbol{\Psi}_{\sigma_i}(\eta) = \begin{bmatrix} \boldsymbol{\Psi}_{\sigma_{xxi}}(\eta) & \boldsymbol{\Psi}_{\sigma_{yyi}}(\eta) & \boldsymbol{\Psi}_{\tau_{xyi}}(\eta) \end{bmatrix}^{\mathrm{T}}$ is the stress mode.

4.2. Linear elastic fracture mechanics with scaled boundary polygons

Within the framework of linear elastic fracture mechanics, the displacement and stress fields for a crack with traction-free surfaces i.e. $\mathbf{F}(\xi) = 0$ are given by Eqs. 42 and (43) with $\mathbf{W}_i^{(\mathrm{p})}(\xi) = 0$ and $\overline{\mathbf{F}}_i^{(\mathrm{w})}(\xi) = 0$. The stiffness matrix is still given by Eq. (40) and the nodal load vector due to side face traction is $\mathbf{R}_{\mathrm{F}} = 0$.

When a crack is modeled by a polygon as shown in Fig. 7b some of the real parts of the eigenvalues of the diagonal blocks in $\mathbf{S}$ satisfy $-1 < \mathrm{Re}(\lambda(\mathbf{S})) < 0$. From Eq. (43), it can be identified that as $\xi \to 0$, the stress field $\boldsymbol{\sigma}(\xi,\eta)$ is dominated by the diagonal blocks in $\mathbf{S}$ with $-1 < \mathrm{Re}(\lambda(\mathbf{S})) < 0$ and leads to a stress singularity. Grouping all the diagonal blocks that satisfy the preceding condition as $\mathbf{S}^{(\mathrm{s})}$, the corresponding displacement modes in $\boldsymbol{\Psi}_{\mathrm{n}}^{(\mathrm{u})}$ as $\boldsymbol{\Psi}^{(\mathrm{s})}$ and integration constants as $\mathbf{c}^{(\mathrm{s})}$, the singular stress field is expressed as

$$\boldsymbol{\sigma}^{(\mathrm{s})}(\xi,\eta) = \boldsymbol{\Psi}_{\sigma}^{(\mathrm{s})}(\eta)\xi^{-\mathbf{S}^{(\mathrm{s})}-\mathbf{I}}\mathbf{c}^{(\mathrm{s})} \tag{44}$$

With this inception, the stress intensity factors can be computed directly from their definitions. For bi-material cracks, the diagonal block $\mathbf{S}^{(\mathrm{s})}$ has a pair of complex conjugate eigenvalues $0.5 \pm i\varepsilon$ where ε is the oscillatory index that depends on the material properties

$$\varepsilon = \frac{1}{2\pi}\ln\left(\frac{\kappa_1/\mu_1 + 1/\mu_2}{\kappa_2/\mu_2 + 1/\mu_1}\right) \tag{45}$$

where μ_i is the shear modulus and

$$\kappa_i = \begin{cases} 3 - 4\nu_i & \text{for plane strain} \\ (3-\nu_i)/(1+\nu_i) & \text{for plane stress} \end{cases} \tag{46}$$

The subscript $i = 1, 2$ denotes the individual material properties of the interface.

When the crack is aligned to the Cartesian coordinate axes as shown in Fig. 7b, the stress intensity factors are defined as [22]

$$\left\{ \begin{array}{c} K_1 \\ K_2 \end{array} \right\} = \sqrt{2\pi\hat{r}} \left[\begin{array}{cc} \cos\left(-\varepsilon \ln \dfrac{\hat{r}}{L}\right) & \sin\left(-\varepsilon \ln \dfrac{\hat{r}}{L}\right) \\ -\sin\left(-\varepsilon \ln \dfrac{\hat{r}}{L}\right) & \cos\left(-\varepsilon \ln \dfrac{\hat{r}}{L}\right) \end{array} \right] \left\{ \begin{array}{c} \sigma_{yy}^{(\mathrm{s})}(\hat{r}, \theta = 0) \\ \tau_{xy}^{(\mathrm{s})}(\hat{r}, \theta = 0) \end{array} \right\} \tag{47}$$

where L is a characteristic length and $\hat{r}$ is the radial coordinate.

Substituting the yy and xy singular stress components into the definition Eq. (47) evaluated at $\xi = 1$ results in

$$\left\{ \begin{array}{c} K_1 \\ K_2 \end{array} \right\} = \sqrt{2\pi l_{\mathrm{OA}}} \left[\begin{array}{cc} \cos\left(-\varepsilon \ln \dfrac{l_{\mathrm{OA}}}{L}\right) & \sin\left(-\varepsilon \ln \dfrac{l_{\mathrm{OA}}}{L}\right) \\ -\sin\left(-\varepsilon \ln \dfrac{l_{\mathrm{OA}}}{L}\right) & \cos\left(-\varepsilon \ln \dfrac{l_{\mathrm{OA}}}{L}\right) \end{array} \right] \left\{ \begin{array}{c} \boldsymbol{\Psi}_{yy}^{(\mathrm{s})}(\eta(\theta = 0)\mathbf{c}^{(\mathrm{s})} \\ \boldsymbol{\Psi}_{xy}^{(\mathrm{s})}(\eta(\theta = 0)\mathbf{c}^{(\mathrm{s})} \end{array} \right\} \tag{48}$$

where l_{OA} is the distance from the crack tip to the polygon boundary shown in Fig. 9a.

4.3. Nonlinear cohesive fracture modeling at the concrete-rock interface with scaled boundary polygons

4.3.1. Cohesive crack model

Along the concrete-rock interface, the fracture is quasi-brittle in nature and is characterised by a fracture process zone in which stress transfer between the concrete and rock surfaces can take place through friction and aggregate interlocking. The fracture process zone along the concrete-rock interface can be modeled by the cohesive crack model, e.g. Barenblatt [33], Dugdale [34], Hillerborg et al. [35]. The cohesive crack model assumes that the fracture process zone can be approximated by consitutive relations that relate the normal and shear cohesive tractions with the relative displacement of the crack faces. This enables the stress transfer across the crack surfaces to be modeled.

The constitutive relations at the process zone are softening functions relating the cohesive tractions to the relative displacement of the crack surfaces. Simplified models that assume linear or bilinear softening have been proposed in the literature e.g. Petersson [36]. Fig. 8a and Fig. 8b shows the bilinear and linear decaying models for the normal and shear cohesive tractions that is used in this study.

In Fig. 8, $t_{\mathrm{n}}^{(\mathrm{u})}$ and $t_{\mathrm{s}}^{(\mathrm{u})}$ are the ultimate tensile and shear strengths of the interface and w_{nc} and w_{sc} are the maximum crack opening and sliding displacements beyond which no normal or shear traction exist. The area under the curves in Fig. 8a and Fig. 8b are the Mode 1 and Mode 2 fracture energies

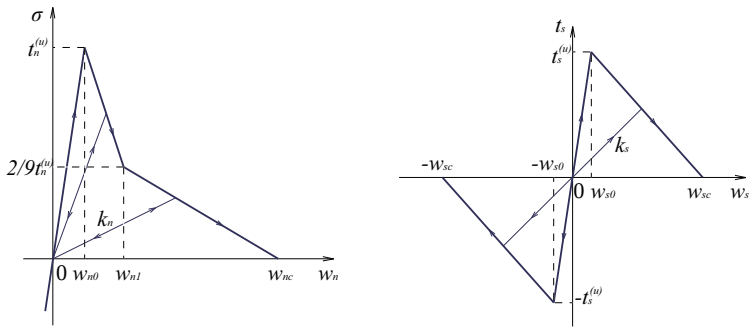

Figure 8: Traction-crack separation law for interface element

G_{f1} and G_{f2} of the interface crack. w_{n0} and w_{s0} are initial thresholds that are introduced to ameliorate the near infinite initial stiffness that may cause difficulties in numerical simulations when w_n and w_s are small. At a point along the process zone, the normal and shear cohesive tractions t_n and t_s are related to the relative opening and sliding displacements on the crack faces w_n and w_s by

$$\left\{ \begin{array}{c} t_s \\ t_n \end{array} \right\} = \left[\begin{array}{cc} k_s & 0 \\ 0 & k_n \end{array} \right] \left\{ \begin{array}{c} w_s \\ w_n \end{array} \right\} \tag{49}$$

where k_n and k_s are the secant stiffness of the softening functions. In Eq. (49), it has been assumed that there is no interaction between t_n and t_s. This assumption is made in this study because a well-defined traction-crack separation law for a concrete/rock interface is not available in literature.

In order to incorporate the cohesive crack model into the scaled boundary polygons (as will be described in Section (4.3.4)), it is convenient to express the normal and shear cohesive tractions t_n and t_s as power functions in terms of the normalized distance from the crack tip to a point on the fracture process zone, ξ, as

$$t_n(\xi) = t_n^{(u)} \sum_{j=1}^{m} e_j \xi^{t_j} \tag{50}$$

$$t_s(\xi) = t_s^{(u)} \sum_{j=1}^{m} g_j \xi^{t_j} \tag{51}$$

with exponents $t_j = j - 1$, $j = 1, 2, ..., m$ and coefficients e_j and g_j.

4.3.2. Interface elements

The cohesive crack model can be implemented using interface elements e.g. Goodman et al. [37], Gerstle and Xie [38]. These elements connect pairs of

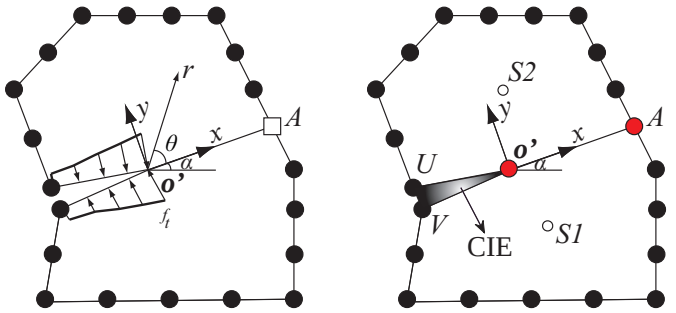

(a) crack polygon subject to cohesive traction

(b) shadow domain of crack polygon

Figure 9: Shadow domain procedure.

nodes on the crack faces. Both normal and shear cohesive tractions can be incorporated. The relationship between the element stiffness matrix $\mathbf{K}_{\mathrm{IE}}$ in local coordinate system is expressed as

$$\mathbf{K}_{\mathrm{IE}} = \frac{A}{2} \sum_{i=1}^{N_{\mathrm{g}}} \mathbf{M}_i^{\mathrm{T}} \mathbf{k}_i \mathbf{M}_i w_i \tag{52}$$

where A is the crack surface area, N_{g} is the number of Gaussian integration points, k_i is the secant modulus in Eq. (49) and $\mathbf{M}_i$ is the shape function matrix. The interface elements can be coupled with the scaled boundary polygons using the shadow domain procedure [25, 28] as will be explained in Section 4.3.

4.3.3. Shadow domain procedure

When cohesive fracture problems are modeled with the scaled boundary finite element method, the cohesive forces that act on the crack faces appear the scaled boundary finite element method equation in displacement (Eq. (5)) as the nonhomogeneous term $\mathbf{F}(\xi)$. The distribution of $\mathbf{F}(\xi)$ is nonlinear because it depends on the relative displacement of the crack faces. In order to use the scaled boundary polygons to model such problems, a two-step approach is adopted.

In the first step, the homogeneous solution of Eq. (5) with $\mathbf{F}(\xi) = 0$ is considered. The cracked polygon is partitioned into two normal polygons as shown in Fig. 9. This mesh is called the shadow domain [28, 25]. The shadow domain discretizes the crack faces and allows the scaled boundary polygons to be coupled to interface elements along the crack path. A nonlinear fracture analysis is then performed using the shadow domain. The interface elements capture the distribution of the cohesive traction at the crack faces t_{n} and t_{s} during the load step.

Although the shadow domain can determine the distribution of t_{n} and t_{s} at the crack faces, accurate information on the asymptotic stress field in the

vicinity of the crack, which is necessary for the evaluation of the stability of a cohesive crack is not readily available. This information is determined from the cracked polygon. The distribution of the cohesive tractions t_{n} and t_{s} are extracted from the interface elements in the shadow domain to determine the nonhomogeneous term $\mathbf{F}(\xi)$. The stress field in the vicinity of the crack is then determined considering the nonhomogeneous term $\mathbf{F}(\xi)$. The resulting stress field is used to determine the stability of the cohesive crack.

4.3.4. Stress field at cohesive crack tip

When t_{n} and t_{s} are expressed as power functions as in Eqs. (50) and (51), the stress field in the cracked polygon $\boldsymbol{\sigma}(\xi,\eta)$ can be computed using Eq. (43) for each j- term by superposition after $\mathbf{F}(\xi)$ has been determined.

To evaluate $\mathbf{F}(\xi)$, the coefficients e_i and g_i in Eqs. (50) and (51) are first computed from the known tractions at the N_g Gaussian integration points on the interface elements, the crack tip and the crack mouth of the cracked polygon. Multiplying Eqs. (50) and (51) with the crack surface area A, the nodal side-face load vector resulting from normal and shear cohesive tractions can be formulated respectively as

$$\mathbf{F}_{t_{\mathrm{n}}}(\xi) = \left(\sum_{j=1}^{m} e_j \xi^{t_j} \right) \mathbf{F}_{t_{\mathrm{n}}} \tag{53}$$

$$\mathbf{F}_{t_{\mathrm{s}}}(\xi) = \left(\sum_{j=1}^{m} g_j \xi^{t_j} \right) \mathbf{F}_{t_{\mathrm{s}}} \tag{54}$$

where $\mathbf{F}_{t_{\mathrm{n}}}$and $\mathbf{F}_{t_{\mathrm{s}}}$ are expressed in global Cartesian coordinates as

$$\mathbf{F}_{t_{\mathrm{n}}} = A t_{\mathrm{n}}^{(\mathrm{u})} \left[\begin{array}{cccccccccc} -\sin\alpha & \cos\alpha & 0 & 0 & \ldots & 0 & 0 & \sin\alpha & -\cos\alpha \end{array} \right]^{\mathrm{T}} \tag{55}$$

$$\mathbf{F}_{t_{\mathrm{s}}} = A t_{\mathrm{n}}^{(\mathrm{u})} \left[\begin{array}{cccccccccc} -\cos\alpha & \sin\alpha & 0 & 0 & \ldots & 0 & 0 & \cos\alpha & -\sin\alpha \end{array} \right]^{\mathrm{T}} \tag{56}$$

and α is the crack angle shown in Fig. 9. Note that only the entries corresponding to the nodes on the crack faces are non-zero.

Using Eqs. (6), (53) and (54), the nonhomogeneous term $\mathbf{F}(\xi)$ in Eq. (5) can be written as

$$\mathbf{F}(\xi) = \left(\sum_{j=1}^{m} e_j \xi^{t_j+1} \right) \mathbf{F}_{t_{\mathrm{n}}} + \left(\sum_{k=1}^{m} g_k \xi^{t_k} \right) \mathbf{F}_{t_{\mathrm{s}}} \tag{57}$$

where each j or k term has the same form as $\mathbf{F}(\xi)$ in Eq. (6).

Once $\mathbf{F}(\xi)$ is known, the complete displacement and stress fields is obtained by simply following the procedures outlined in Sections 4.1.4 and 4.1.5.

4.3.5. Stability of cohesive crack

Research on the stability of bi-material interface cracks with cohesive traction subjected to mixed-mode loading is scarce. A universal criterion to determine its stability has not been agreed on. In this paper, it is proposed that the bi-material interface crack will propagate when the stress intensity factors evaluated by Eq. (48) satisfy the following condition:

$$K_1 = 0 \text{ or } K_2 = 0 \tag{58}$$

This criterion is similar to enforcing the zero-K condition [39, 24] i.e. the stress at the crack has to be finite (i.e. there is no stress singularity).

Both K_1 and K_2 has to be considered for bi-material interface cracks because the magnitudes of the tensile and shear cohesive tractions are of the same order. This is in contrast to a homogeneous crack in which its stability can be sufficiently determined by considering K_1 only.

4.4. Crack propagation modeling

The simple remeshing algorithm shown in Fig. 10 is used to model crack propagation. Remeshing can be carried out by simply splitting the cracked polygon into two and updating the location of the crack tip in the mesh. This algorithm is described in detail using the mesh shown in Fig. 10a as an example. In this figure, the cracked polygon is defined by the vertices 1-2-3-4-5-6-7-8-9 surrounding the crack tip O.

When the crack propagation criterion is met, the crack is assumed to propagate along the interface. The crack propagation length is assumed to be approximately the size of one polygon, i.e., the crack tip moves from the current position to the scaling center of the next polygon along the interface. Remeshing is carried out according to the following steps:

1. Split the current crack polygon into two normal polygons (Fig. 10b). The current crack tip is split into two vertices 15 and 16 Fig 10b. The intersection of the edge at the crack front with the interface, i.e., vertex 5, is split into vertices 17 and 18. This splits the crack polygon into two new polygons defined by vertices 9-16-18-6-7-8 and 1-2-3-4-17-15 with scaling centres O_3 and O_4, respectively.
2. Generation of new crack polygon (Fig. 10c). The two polygons at the crack front, with scaling centers O_1 and O_2 respectively, are merged into one polygon. The scaling center is located at the new crack tip O'. The original edge 5-12 is deleted. Two new side faces, $O'-17$ and $O'-18$, are generated.
3. Insertion of interface elements (Fig. 10d). Interface elements are inserted between the newly-formed crack faces, i.e., 16-18, 15-17, $O'-17$ and $O'-18$ after its shadow domain is generated. For each pair of edges along the crack path, one interface element is inserted. In each interface element, the fracture process zone of the concrete-rock interface is modelled by the cohesive crack model and coupled to the scaled boundary finite element

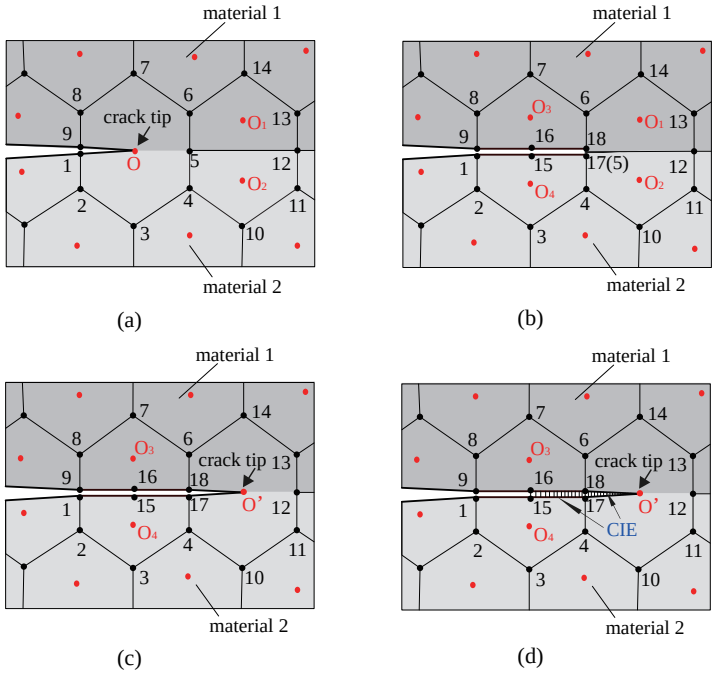

Figure 10: Remeshing during crack propagation

method through the shadow domain procedure depicted in Sections 4.3.1 and 4.3.3, respectively.

For crack propagation along a bi-material interface, the number of polygons remains unchanged. Only three additional vertices are generated during the remeshing process. The remeshing procedure is therefore very simple and straight forward. If the crack kinks into either material 1 or material 2, with the propagation angle determined, the procedure proposed by Ooi et al. [29], for example, can be employed after some augmentation.

5. Evaluation of mode mixity, fracture toughness and fracture energy

The dependency of the fracture toughness, K_{1c} and K_{2c} and the fracture energy, Γ of the concrete-rock interface with the mode-mixity ψ is investigated in this section. The scaled boundary polygons are used to compute K_{1c}, K_{2c}, Γ and ψ from the experimentally measured peak loads under the assumption of linear elastic fracture mechanics.

5.1. Quantification of composite beams according to mode mixity

To facilitate the discussion on the interface fracture behaviour of concrete and rock with respect to the mode-mixity, it is useful to first quantify the

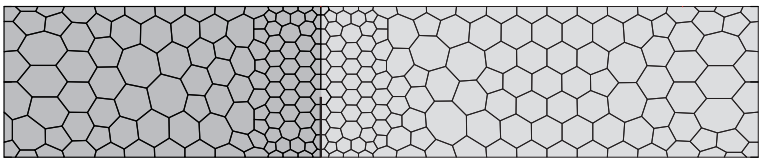

Figure 11: Composite beam discretized by scaled Boundary polygons ($L_{\text{rock}} = 210$mm).

composite beam specimens according to their mode mixity angles ψ. The mode mixity angle is defined as

$$\psi = \arctan\left(K_2/K_1\right) \tag{59}$$

The mode mixity angle are evaluated using the scaled boundary polygons under the assumption of linear elastic fracture mechanics. The composite beam is discretized using polygon meshes. Fig. 11 shows the polygon mesh of the specimen with $L_{\text{rock}} = 210$mm. The mesh has 268 polygons and 677 nodes. The polygon meshes of the other specimens have similar number of polygons and nodes. The material properties of concrete and rock follow from that listed in Table 1. Plane strain conditions are assumed. The boundary conditions follow from that in Fig. 1. The stress intensity factors K_1 and K_2 are evaluated from Eq. (48). The characteristic length L was assumed to be 40mm i.e. the length of the preset crack. The mode mixity angle were computed using Eq. (59).

The mode mixity angles ψ of the composite beams are reported in the third column in Table 3. Specimens with high magnitudes of ψ are said to be shear dominated. It is clear from Table 3 that the mode mixity angle covered the range from near pure shearing to near pure opening. It needs to be emphasized that the current experiment setup only covers the case of negative shear stress. However, since the material mismatch between concrete and rock is not prominent, symmetry with respect to the shear component can be assumed with negligible influence.

5.2. Interface fracture toughness

The interface fracture toughness $K_{1\text{c}}$ and $K_{2\text{c}}$ were evaluated from the experimentally measured peak loads $P^{\max}$ and Eq. (48) using the scaled boundary polygons. The polygon meshes used to compute ψ in Section 5.1 were used. Both $K_{1\text{c}}$ and $K_{2\text{c}}$ were computed under the assumption that the theory linear elastic fracture mechanics holds [8].

Table 3 lists the fracture toughness of all the specimens tested in the experiment. The variation of $K_{1\text{c}}$ and $K_{2\text{c}}$ with the mode mixity angle ψ is plotted in Fig. 12a. It is apparent from Fig. 12a that the magnitudes of $K_{1\text{c}}$ decreases as the magnitude of ψ increases. On the other hand $K_{2\text{c}}$ increases as the magnitude of ψ increases. For the shear dominant specimens, $K_{2\text{c}}$ did not increase to

Table 3: Mode mixity, fracture toughness and energy release rates of composite beams.

Specimen	L_{rock} (mm)	ψ (deg)	K_{1c} (MPa$\sqrt{\text{m}}$)	K_{2c} (MPa$\sqrt{\text{m}}$)	G_c (N/m)
210-2	210	-8.5	0.51	-0.08	11.25
210-3			0.56	-0.08	13.66
210-4			0.80	-0.12	27.77
215-1	215	-12.5	0.67	-0.15	19.77
215-2			0.84	-0.19	31.52
215-3			0.75	-0.17	24.89
215-4			0.85	-0.19	31.99
220-1	220	-17.1	0.85	-0.26	33.35
220-2			0.40	-0.12	7.25
220-3			0.60	-0.18	16.53
220-4			0.59	-0.18	16.11
225-2	225	-22.6	0.52	-0.22	13.50
225-3			0.27	-0.11	3.69
225-4			0.77	-0.32	29.35
230-3	230	-29.4	0.55	-0.31	16.97
230-4			0.72	-0.41	28.81
235-3	235	-38.1	0.76	-0.60	39.21
235-4			0.61	-0.48	25.19
240-2	240	-49.5	0.49	-0.58	24.40
240-4			0.47	-0.55	21.85
245-1	245	-64.5	0.39	-0.81	34.16
245-3			0.29	-0.61	19.53
245-4			0.32	-0.67	23.54
250-1	250	-82.4	0.10	-0.77	25.16
250-4			0.08	-0.56	13.64

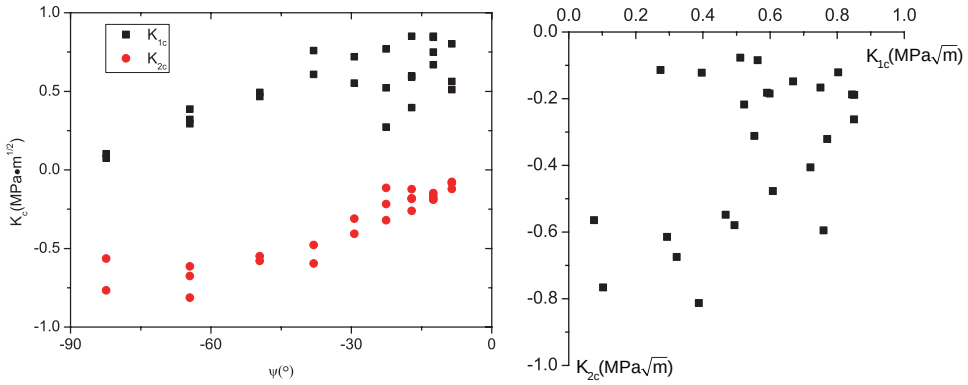

(a) Fracture toughness vs. mode mixity angle

(b) K_{1c} vs. K_{2c}

Figure 12: Interfacial fracture toughness.

a significantly large value. This can be explained by the failure modes IR and IC that are usually observed in these specimens during the experiment. The kinking of the crack into the rock or the development of a secondary crack near the concrete support suggests that there is a relatively stronger resistance along the interface. The measured $P^{\max}$ is therefore lower than it would had been if the crack had propagated along the interface. The predicted K_{2c} is therefore, lower than the case where the crack propagates along the interface. The relation between K_{1c} and K_{2c} are plotted in Fig 12b. The scattered data points roughly formed a quarter of a circle.

It is worth mentioning that for cases of small mode mixity angles, the points for K_{1c} seemed to be equally scattered between $K_{1c} = 0.5 \sim 0.8\text{MPa}\sqrt{\text{m}}$. It indicates that for magnitudes of ψ, its influence on the critical stress intensity factors is negligible. Therefore, the critical stress intensity factors are nearly constant.

5.3. Interface fracture energy

The fracture energy Γ characterizes the fracture resistance of the interface. It can be obtained by calibrating the energy release rate G that is obtained experimentally from test specimens. The energy release rate G that is required for a crack to propagate along the interface can be expressed as [6]

$$G = \frac{1/\overline{E}_1 + 1/\overline{E}_2}{2\cosh^2(\pi\varepsilon)} \left(K_1^2 + K_2^2\right) \tag{60}$$

where ε is the oscillatory index as defined in Eq. (45) and

$$\overline{E}_j = \begin{cases} E_j/(1-\nu_j^2) & \text{plane strain} \\ E_j & \text{plane stress} \end{cases} \tag{61}$$

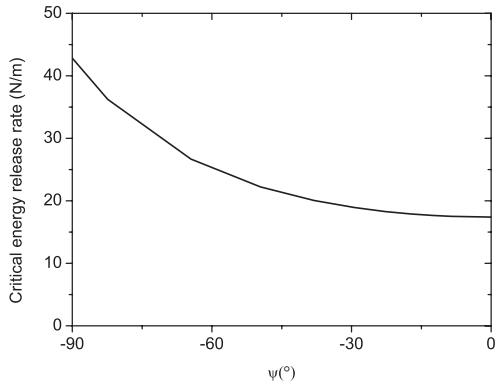

Figure 13: Variation of Γ with ψ.

E_j and ν_j are the Young's modulus and Poisson's ratio of the materials at the interface crack. The subscript $j = 1, 2$ denotes the material of the bi-material interface. Using the K_{1c} and K_{2c} in Table 3 and Eq. (60), the energy release rates of the specimens can be calculated. The results are listed in column six of Table 3.

For bi-material interface cracks, the interfacial fracture energy Γ is dependent on the mode mixity angle ψ. In this study, Γ is assumed to be related to ψ by the relation

$$\Gamma(\psi) = G_{Ic} \left\{1 + \tan^2 \left[(1 - \lambda)\psi\right]\right\} \tag{62}$$

that was proposed by Kinloch [40]. The parameters G_{Ic} and λ are determined by nonlinear data fitting. Using the results in Table 3 with $\Gamma = G_c$, G_{Ic} and λ were found to be $G_{Ic} = 17.4$N/m and $\lambda = 0.44$. The expression for the interfacial fracture energy of the concrete-rock interface crack used in this study is

$$\Gamma(\psi) = 17.4 \left[1 + \tan^2 (0.56\psi)\right] \tag{63}$$

A plot of Eq. (63) is shown in Fig. 13. From Fig. 13, it is found that the interface fracture energy for pure Mode 2 i.e. $\psi = -90°$ is about 2.5 times the interface fracture energy for pure Mode 1 i.e. $\psi = 0°$. The relation in Eq. (63) indicates that Γ increases as ψ increases.

6. Nonlinear fracture analysis of concrete-rock interface

In this section, the fracture behaviour of the concrete-rock interface is investigated by nonlinear fracture mechanics using the scaled boundary polygons. The material parameters of the cohesive traction-separation laws are determined from the experimental measurements and the scaled boundary polygons by calibration. Cohesive crack propagation in the concrete-rock specimens is then

modeled. The predicted $P-$CMOD and $P-$CMSD responses are validated using the experimental measurements.

6.1. Calibration of cohesive crack model parameters of concrete-rock interface

The parameters of the cohesive crack model for the concrete-rock interface are determined by calibrating the experimental measurements with the numerical simulations. Assuming that the cohesive traction-separation laws for normal and shear are of the forms shown in Figs.8a and 8b, six independent parameters i.e. the Mode 1 fracture energy G_{f1}, the Mode 2 fracture energy G_{f2}, the tensile strength $t_{\mathrm{n}}^{(\mathrm{u})}$, the shear strength $t_{\mathrm{s}}^{(\mathrm{u})}$ and the two thresholds w_{n0} and w_{s0} for the ascending sections of the traction separation curves have to be determined.

The initial separation thresholds w_{n0} and w_{s0}, which is necessary for numerical implementation (as explained in Section 4.3.1), are both selected to be 0.001mm in this study. G_{f1} and $t_{\mathrm{n}}^{(\mathrm{u})}$ are determined by calibrating the results from the tensile dominant specimen ($L_{\mathrm{rock}} = 210$mm) with the numerical simulations. G_{f2} and $t_{\mathrm{s}}^{(\mathrm{u})}$ are determined from the results for the shear dominant specimen ($L_{\mathrm{rock}} = 250$mm). The parameters obtained from the calibration process are listed in Table 4.

Table 4: Parameters for traction separation curves.

$t_{\mathrm{n}} - w_{\mathrm{n}}$	G_{f1}(N/m)	$t_{\mathrm{n}}^{(\mathrm{u})}$(MPa)	w_{n0}(mm)
	100	2.0	0.001
$t_{\mathrm{s}} - w_{\mathrm{s}}$	G_{f2}(N/m)	$t_{\mathrm{s}}^{(\mathrm{u})}$(MPa)	w_{s0}(mm)
	200	3.5	0.001

6.2. Validation of numerical simulations

Crack propagation in the bi-material specimens tested are modeled using the scaled boundary polygons. The material properties of concrete and rock tabulated in Table 1 are used as inputs. The cohesive crack models with the parameters determined in Table 4 is used to model the fracture process zone at the concrete-rock interface. The same polygon meshes used in Section 5 are used for the simulations. The numerical simulations were validated by the experimental measurements.

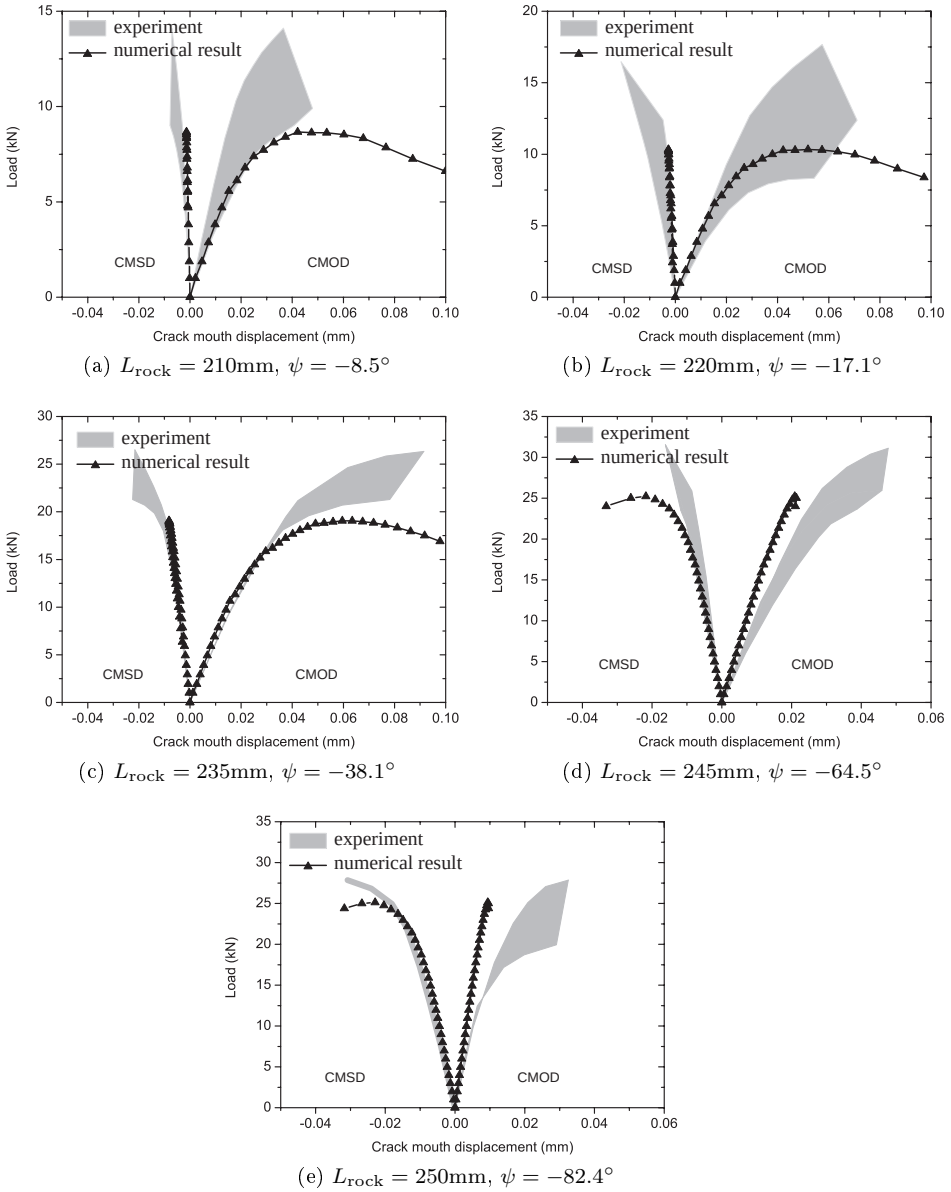

(a) $L_{\text{rock}} = 210\text{mm}$, $\psi = -8.5°$

(b) $L_{\text{rock}} = 220\text{mm}$, $\psi = -17.1°$

(c) $L_{\text{rock}} = 235\text{mm}$, $\psi = -38.1°$

(d) $L_{\text{rock}} = 245\text{mm}$, $\psi = -64.5°$

(e) $L_{\text{rock}} = 250\text{mm}$, $\psi = -82.4°$

Figure 14: Load-crack mouth displacement curves.

Fig. 14 shows the load-crack mouth opening displacement ($P-\text{CMOD}$) and load-crack mouth sliding displacement ($P-\text{CMSD}$) curves of the specimens with $\psi = -8.5°, -17.1°, -38.1°, -64.5°$ and ,$-82.4°$. Generally, the numerically predicted $P-\text{CMOD}$ curves agree reasonably well with the experimental measurements.

For the case of $\psi = -8.5°$, the Mode 1 component is always dominant at the crack tip. The CMOD is about ten times larger than the CMSD. When the mode mixity angle is increased, the influence of the Mode 2 stress component at the crack tip becomes more apparent. Correspondingly, the CMSD increases while the CMOD decreases. For the case of $\psi = -82.4°$, the magnitude of the CMSD is approximately two times larger than the CMOD.

For the tensile dominant specimens, e.g. $\psi = -8.5°$ and $\psi = -17.1°$, a wide and stable plateau is observed in the experimentally measured and numerically simulated $P -$ CMOD curves after the peak load has been reached (Figs. 14a – 14c). This reflects a significant amount of ductility and strong nonlinearity of the interface. This observation highlights the importance of incorporating the cohesive crack model in the numerical simulations to enable the nonlinear fracture behavior at the concrete-rock interface to be captured more realistically.

For the shear dominant specimens, e.g. $\psi = -64.5°$ and $\psi = -82.4°$, there is no clear indication that a plateau developed in $P -$ CMSD. Some degree of nonlinearity was observed in the $P -$ CMSD curves after the peak load has been reached and the specimens failed when the specimen was further loaded. The numerical simulations were able to capture the strain-softening behaviour at the interface in the $P -$ CMSD curves. This phenomenon was not observed in the experimental measurements.

The numerically predicted peak loads agreed very well with the experimental measurements. For example, the predicted peak loads $P^{\max}$ for the specimens with $\psi = -8.5°$and $\psi = -82.4°$ are 8.66kN and 25.13kN, respectively. The experimental $P^{\max}$ were in the range of 8.97kN $-$ 14.09kN for $\psi = -8.5°$ and 20.41kN $-$ 27.71kN for $\psi = -82.4°$. The peak load for the shear dominant specimen is about three times of that in the tensile dominant specimen, which is consistent with the increase of Γ with ψ observed in Section 5.3.

Fig. 15 shows the variation of the experimentally measured and numerically predicted peak loads $P^{\max}$ with the mode mixity angle ψ. The peak load increased when the mode mixity angle ψ was increased. In specimens with large mode mixity angles ψ, the load bearing capacity of the specimen increased because of the increase in the magnitude of the K_2 near the crack tip. This created a crack shielding effect which delayed the crack propagation. The plot in Fig. 15 indicated that $P^{\max}$ increased by approximately three times when the mode mixity angle ψ was increased from $-8.5°$ to $-38.1°$. The magnitude of $P^{\max}$ does not significantly increase when ψ was further increased to $-82.4°$.

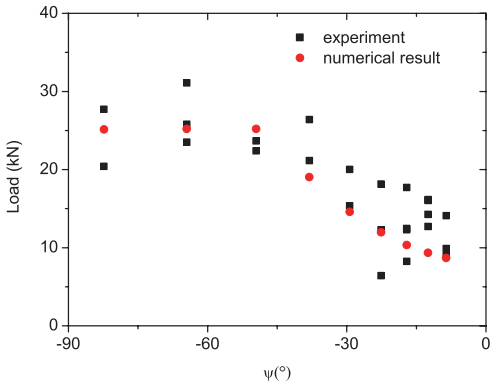

Figure 15: Variation of $P^{\max}$ with mode mixity angle ψ.

In the shear dominated specimens, the magnitude of the tensile stress component caused by external loading is negligible compared to the shear stress component (indicated by the small CMOD values in Fig. 14e). From the sign of K_2 reported in Table 3, the crack has a strong tendency to deflect into the rock. At the same time, the magnitude of the bending moment and the shear force at the right support also increase when the external load is increased. This explains the frequency of the IC and IR failure modes observed in these specimens. This phenomenon also leads to an underestimation of the fracture toughness at high mode mixity angles.

The crack propagation process of the specimens with $\psi = -8.5°$, $\psi = -38.1°$ and $\psi = -82.4°$ are plotted in Figs. 16-18, respectively. The black lines in the left and right meshes represent the normal and shear cohesive traction distribution at a particular load step. In all the three specimens, the crack mouths remain open as the load increases. The fracture process zone is present throughout the entire loading, indicating that it has yet to fully develop in the specimens.

For the tensile dominated specimen i.e. $\psi = -8.5°$ shown in Fig. 16, the magnitude of the normal traction t_{n} on the cracks faces decreases as the crack propagates. However, the shear traction t_{s} remains equal to the shear strength ($t_{\mathrm{s}}^{(\mathrm{u})} = 3.5\mathrm{MPa}$) throughout the entire simulation. This indicates that the sliding between the crack faces is small. For the shear dominated specimen i.e. $\psi = -82.4°$ shown in Fig. 18, the shear traction t_{s} on the crack faces decreases as the crack propagates. However, the normal traction t_{n} remains equal to the tensile strength ($t_{\mathrm{n}}^{(\mathrm{u})} = 2.0\mathrm{MPa}$), which indicates that the opening of the crack faces is very small. For the specimens where neither the tensile or shear mode dominates i.e. $\psi = -38.1°$ shown in Fig. 17, both t_{s} and t_{n} decrease as the crack propagates.

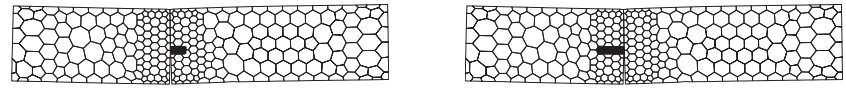

(a) $P = 5.57$kN

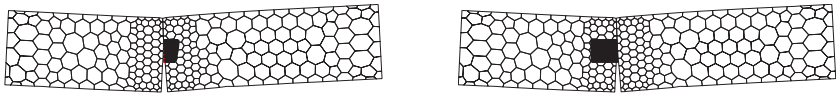

(b) $P = 8.66$kN

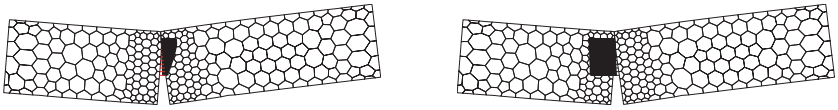

(c) $P = 7.25$kN

Figure 16: Crack propagation process and cohesive traction distribution (left-tension, right-shear) of composite beam with $\psi = -8.5°$.

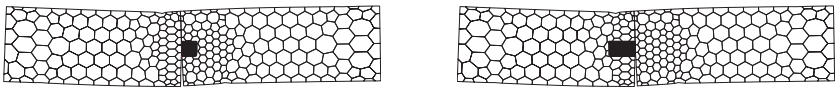

(a) $P = 12.15$kN

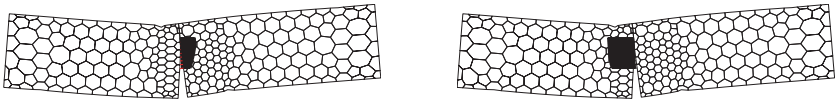

(b) $P = 19.05$kN

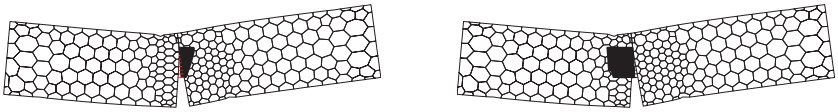

(c) $P = 17.51$kN

Figure 17: Crack propagation process and cohesive traction distribution (left-tension, right-shear) of composite beam with $\psi = -38.1°$.

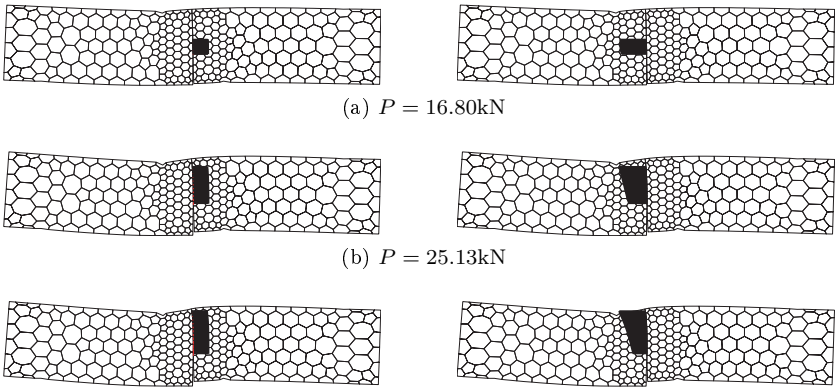

(a) $P = 16.80$kN

(b) $P = 25.13$kN

(c) $P = 24.39$kN

Figure 18: Crack propagation process and cohesive traction distribution (left-tension, right-shear) of composite beam with $\psi = -82.4°$

Fig. 19 shows the crack lengths of the specimens when $P = P^{\max}$. It can be clearly seen that the cohesive crack length increases as the mode mixity increases. Since for all specimens, the fracture process zones are not developed to the full length, the magnitude of the cohesive traction in the cracks is generally high. The longer cohesive cracks indicate the load bearing capacity at the interface has yet to be exhausted. This phenomenon could contribute partly to the higher peak load for specimens with high mode mixity ratio.

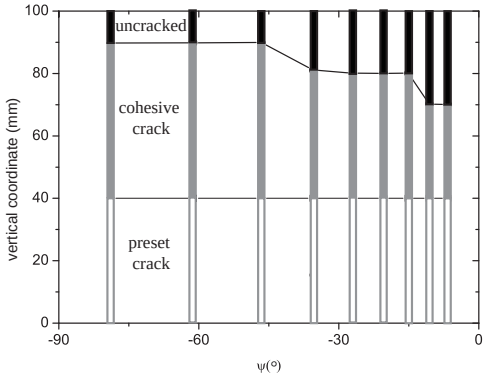

Figure 19: Crack profile at peak loads.

7. Conclusions

The dependency of the fracture behaviour of concrete-rock interface crack on the mode mixity ratio has been investigated. Four-point shear tests were performed on a series notched concrete-rock composite beams. The specimens were designed so that a wide range of mode mixity angle (from almost pure shear

to almost pure tensile loading) can be tested. To interpret the experimental results, the scaled boundary polygon formulation, which is well-known for its accuracy in fracture analysis, is used to compute the fracture toughness and the fracture energy at the concrete-rock interface and to model the nonlinear fracture behaviour. The numerical simulations were successfully validated using the experimental measurements. From this study, it was found that:

1. The mode mixity angle ψ affects the failure mode at the concrete-rock interface. Specimens with low magnitudes of ψ were observed to fail due to cracking along the concrete-rock interface. In specimens with high magnitudes of ψ, the crack showed a tendency to kink into the rock after initial cracking along the interface.
2. The fracture energy Γ of the concrete-rock interface increases when the magnitude of ψ increases. For the materials tested, fracture energy under shear dominant condition is 2.5 times of the tensile dominant case.
3. Nonlinear crack propagation simulations showed that specimens with low ψ showed a significant amount of ductility, which reflected the strong nonlinearity of the interface. In specimens with high magnitudes of ψ, only a small degree of nonlinearity was observed in the loading response.

It is well-known that scale effects exist in structures made of quasi-brittle materials such as the concrete-rock interface considered in this study. The experimental program presented in Section 2 can, in the near future, be repeated with specimens of different sizes in order to investigate the effects of scale that govern the problem.

Acknowledgements

This study was supported by the Australian Research Council through grant number DP120100742, by the National Science Foundation of China through Grant number 51009019.

References

References

[1] B. K. Atkinson, Fracture mechanics of rock, Academic Press, London, 1989.

[2] S. Kumar, S. V. Barai, Concrete fracture models and applications, Springer, Berlin, Heidelberg, 2011.

[3] Design specification for concrete gravity dams, Ministry of Water Resources of the People's Republic of China, 2005.

[4] J. W. Chavez, G. L. Fenves, Earthquake analysis of concrete gravity dams including base sliding, Earthquake Engineering and Structural Dynamics 24 (1995) 673–686.

[5] F. Javanmardi, P. Leger, R. Tinawi, Seismic structural stability of concrete gravity dams considering transient uplift pressures in cracks, Engineering Structures 27 (2005) 616–628.

[6] J. W. Hutchinson, Z. Suo, Mixed mode cracking in layered materials, Advanced in Applied Mechanics 29 (1992) 63–191.

[7] K. M. Lee, O. Buyukozturk, Fracture analysis of mortar-aggregate interfaces in concrete, ASCE Journal of Engineering Mechanics 118 (1992) 2031–2047.

[8] K. M. Lee, O. Buyukozturk, Fracture toughness of mortar-aggregate interface in high-strength concrete, ACI Structural Journal 92 (1995) 634–642.

[9] O. Buyukozturk, B. Hearing, Crack propagation in concrete composites influenced by interface fracture parameters, International Journal of Solids and Structures 35 (1998) 4055–4066.

[10] H. V. Tippur, A. J. Rosakis, Quasi-static and dynamic crack growth along bimaterial interfaces: A note on crack-tip field measurements using coherent gradient sensing, Experimental Mechanics 31 (1991) 243–251.

[11] H. V. Tippur, S. Ramaswamy, Measurement of mixed-mode fracture parameters near cracks in homogeneous and bimaterial beams, International Journal of fracture 61 (1993) 247–265.

[12] A. Agrawal, A. M. Karlsson, On the reference length and mode mixity for a bimaterial interface, ASME Journal of Engineering Materials and Technology 129 (2007) 580–587.

[13] S. C. Yang, S. Li, Z. Li, S. M. Huang, Experimental investigation on fracture toughness of interface crack for rock/concrete, International Journal of Modern Physics B 22 (2008) 6141–6148.

[14] C. F. Shih, R. J. Asaro, Elastic-plastic analysis of cracks on bimaterial interfaces: Part I - small scale yielding, Journal of Applied Mechanics 55 (1988) 299–316.

[15] P. P. L. Matos, R. M. McMeeking, P. G. Charalambides, M. D. Drory, A method for calculating stress intensities in bimaterial fracture, International Journal of Fracture 40 (1989) 235–254.

[16] K. Y. Lin, J. W. Mar, Finite element analysis of stress intensity factors for cracks at a bi-material interface, International Journal of Fracture 12 (1976) 521–531.

[17] N. Sukumar, Z. Y. Huang, J. H. Prevost, Z. Suo, Partition of unity enrichment for bimaterial interface cracks, International Journal for Numerical Methods in Engineering 59 (2004) 1075–1102.

[18] M. L. Williams, The stress around a fault or crack in dissimilar media, Bulletin of the Seismology Society of America 49 (1959) 199–204.

[19] B. L. Karihaloo, Q. Z. Xiao, Asymptotic fields at the tip of a cohesive crack, International Journal of Fracture 150 (2008) 55–75.

[20] A. Alberto, S. Valente, Asymptotic fields at the tip of a cohesive frictional crack growing at the bi-material interface between a dam and the foundation rock, Engineering Fracture Mechanics 108 (2013) 152–161.

[21] J. P. Wolf, The scaled boundary finite element method, John Wiley & Sons Inc, 2003.

[22] C. Song, F. Tin-Loi, W. Gao, A definition and evaluation procedure of generalized stress intensity factros at cracks and multi-material wedges, Engineering Fracture Mechanics 77 (2010) 2316–2336.

[23] P. O. Bouchard, F. Bay, Y. Chastel, Numerical modeling of crack propagation - implementation techniques and comparison of different criteria, Computer Methods in Applied Mechanics and Engineering 192 (2003) 3887–3908.

[24] N. Moes, T. Belytschko, Extended finite element method for cohesive crack growth, Engineering Fracture Mechanics 69 (2002) 813–833.

[25] E. T. Ooi, C. Song, F. Tin-Loi, Automatic modeling of cohesive crack propagation in concrete using polygon scaled boundary finite element., Engineering Fracture Mechanics 93 (2012) 13–33.

[26] F. Barpi, S. Valente, The cohesive frictional crack model applied to the analysis of the dam-foundation joint, Engineering Fracture Mechanics 77 (2010) 2182–2191.

[27] C. Song, Analysis of singular stress fields at multi-material corners under thermal loading., International Journal for Numerical Methods in Engineering 65 (2006) 620–652.

[28] Z. J. Yang, A. J. Deeks, Fully-automatic modeling of cohesive crack growth using a finite element-scaled boundary finite element coupled method., Engineering Fracture Mechanics 74 (2007) 2547–2573.

[29] E. T. Ooi, C. Song, F. Tin-Loi, Scaled boundary polygon finite element for crack propagation modeling., International Journal for Numerical Methods in Engineering 91 (2012) 319–342.

[30] M. Y. He, H. C. Cao, A. G. Evans, Mixed-mode fracture: the four-point shear specimen, Acta Metallurgica et Materialia 38 (1990) 839–846.

[31] A. Carpinteri, S. Valente, G. Ferrara, G. Melchiorri, Is mode II fracture energy a real material property?, Computers and Structures 48 (1992) 397–413.

[32] A. J. Deeks, J. P. Wolf, A virtual work derivation of the scaled boundary finite-element method for elastostatics, Computational Mechanics 28 (2002) 489–504.

[33] G. Barenblatt, The mathematical theory of equilibrium cracks in brittle fracture., Advances in Applied Mechanics 7 (1962) 55–129.

[34] D. Dugdale, Yielding of steel sheets containing slits., Journal of the Mechanics and Physics of Solids 8 (1960) 100–104.

[35] A. Hillerborg, M. Modeer, P. E. Petersson, Analysis of crack formation and crack growth in concrete by means of fracture mechanics and finite elements., Cement and Concrete Research 6 (1976) 773–782.

[36] P. E. Petersson, Crack growth and development of fracture zone in plain concrete and similar materials., Tech. Rep., Lund Institute of Technology, Sweden, 1981.

[37] R. E. Goodman, R. L. Taylor, T. L. Berkke, A model for the mechanics of jointed rock., ASCE Journal of the Soil Mechanics Division 99 (1968) 637–659.

[38] W. Gerstle, M. Xie, FEM modeling of fictitious crack propagation concrete., ASCE Journal of Engineering Mechanics 118 (1992) 416–434.

[39] Z. P. Bazant, N. Y. Li, Stability of cohesive crack model: Part 1 - energy principles., ASME Journal of Applied Mechanics 62 (1995) 959–964.

[40] A. J. Kinloch, Adhesion and adhesives, Chapman and Hall, 1987.